

Polyaniiline modified bimetallic hydroxide/ZIF composites as electrode materials for supercapacitors with high capacity and high stability

Jinyue Yang^a, Jianxin Wang^{b,c,*}, Chunhua Lou^b, Yuhua Cui^d, Xin Huang^b, Haixia Yu^a, Liming Bai^a, Wendi Wang^a, Xinyou Zhang^a, Hong Pan^{a,**}

^a College of Chemistry and Chemical Engineering, Qiqihar University, Qiqihar, Heilongjiang Province 161000, China

^b College of Materials Science and Engineering, Qiqihar University, Qiqihar, Heilongjiang Province 161006, China

^c Heilongjiang Provincial Key Laboratory of Polymeric Composition Materials, Qiqihar, Heilongjiang Province 161006, China

^d School of Chemistry and Environmental Engineering, Changchun University of Science and Technology, Jilin, Changchun Province, 130022, China



ARTICLE INFO

Keywords:

Metal-organic framework
Supercapacitors
PANI
Cyclic stability

ABSTRACT

Metal-organic framework materials (MOFs) are widely used in electrochemical energy storage due to their abundant active sites and high redox activity. Especially in the field of supercapacitors, the porous structure of MOFs makes them the most promising candidates for composite electrode materials due to their vast specific surface area. However, the poor chemical stability of MOFs in alkaline electrolytes limits their application. Constructing and improving the stability of metal-organic backbone materials through rational structural design is the key to enhancing the electrochemical performance of capacitors. In this paper, the stability of ZIF-67 was enhanced by the complexing with bimetallic hydroxide (CoMn-LDH), and the conductivity is further enhanced by the mixing of polyaniline (PANI) to form a ``network structure'' morphology. As a result, the composite electrode material has a specific capacity of 1048 F g^{-1} at 1 A g^{-1} with a good cycle life (80.5 % capacity retention for 5000 cycles). The specific capacity of the CoMn-LDH/ZIF-67/PANI//AC asymmetric supercapacitor (ASC) was 164 F g^{-1} at 1 A g^{-1} in the voltage range of 0–1.5 V. The maximum energy density of the ASC was 51.25 Wh kg^{-1} at a power density of 2250 W kg^{-1} . In addition, excellent cycling stability (71.2 % capacitance retention after 5000 cycles) was delivered.

1. Introduction

Facing the continuously growing energy demand, as well as the rapid decrease of traditional non-renewable energy sources [1–4], new energy sources and low energy-consuming storage technologies are receiving more attention. Among them, supercapacitors play an essential role in electrical energy storage due to their advantages of sample energy storage, fast charging and discharging, long cycle life, and wide operating temperature [5–8]. The electrode material is an integral part of the supercapacitor and directly determines the performance of the supercapacitor [9,10]. The pseudo-capacitive materials can store charges on the entire electrode surface and inside simultaneously, and their capacitance can be up to tens of times that of the capacitor simply employs double-layer electrode materials. Metal oxides, metal hydroxides [11–13], metal sulfides [14], metal phosphides [15,16] metal-organic skeletons (MOFs), and their hybrid materials are commonly used

electrode materials. Among them, MOFs have been widely used in capacitors due to their ultra-high specific surface area, periodic structure, good crystallinities, and tunable chemical components. Zeolite imidazolium salt frameworks (ZIFs), as a subclass of MOFs are particularly attractive in the field of supercapacitors due to their adjustable porosity, high crystallinity, and functionalization properties. However, the insulating nature of the organic ligands and the coordination of the d-orbitals of the metal ions with the organic ligands prevent effective delocalization of the electrons across the frameworks, resulting in poor electrical conductivity of most of the ZIFs materials [17–21]. The disadvantages can be overcome by preparing derivatives of the ZIFs materials. Derivatives of ZIFs materials can not only maintain the advantages of ZIFs but also effectively improve the electrical conductivity of ZIFs materials. Zhang et al. [22] used ZIF-67 as a sacrificial template to design hollow porous rhombic dodecahedral Co_3O_4 , which retained the porous skeleton of ZIFs, and obtained excellent capacitance.

* Corresponding author at: College of Materials Science and Engineering, Qiqihar University, Qiqihar, Heilongjiang Province 161006, China.

** Corresponding author.

E-mail addresses: wjx666929@163.com (J. Wang), 03211@qqrhu.edu.cn (H. Pan).

However, the drawback of poor stability still exists. ZIFs can be etched by hydroxides in the alkaline electrolyte and release metal cations. It usually leads to structural collapse, and ultimately results in a rapid decay of the surface capacitance contribution and poor electrode material lifetime. Layered bimetallic hydroxides (LDHs) are classical two-dimensional materials with excellent ion exchange and intercalation capabilities, as well as high redox activity and tunable chemical compositions [23–27]. LDHs have a relatively weak interlayer bonding force, so it has a strong ability to trap organic and inorganic ions and can be used as ion acceptors.

In this work, a high-capacitance supercapacitor based on ZIF67, CoMn-LDH, and PANI was synthesized. CoMn-LDH can accept Co^{2+} dissolved from the ZIF-67 skeleton to improve the utilization of the metal-organic framework in alkaline electrolytes. In addition, the high conductivity of PANI facilitates rapid charge through from the overall electrode material. The individual ZIF-67/CoMn-LDH nanoparticles are connected by conductive polymers, forming a cross-linked conductive network. It facilitates the transport of electrons on the outer surface and inside the ZIFs material. As a result, CoMn-LDH/ZIF-67/PANI electrode material with layered porous structure showed excellent electrochemical properties. CoMn-LDH/ZIF-67 showed higher stability than pure ZIF-67. Moreover, due to the introduction of the highly conductive network of PANI, CoMn-LDH/ZIF-67/PANI showed significantly higher capacity than the CoMn-LDH/ZIF-67 composite without PANI. As a result, the power/energy density of the supercapacitors composed of CoMn-LDH/ZIF-67/PANI and activated carbon (AC) reached 2250 W kg^{-1} and 51.25 Wh kg^{-1} , respectively. These results indicate that CoMn-LDH/ZIF-67/PANI is a promising electrode material with potential applied value in supercapacitors.

2. Experimental section

2.1. Materials and reagents

Cobalt nitrate hexahydrate ($\text{Co}(\text{NO}_3)_2 \bullet 6\text{H}_2\text{O}$), 2-methylimidazole (MEIM), cetyltrimethylammonium bromide (CTMAB), N,N-dimethylformamide (DMF), and activated carbon (AC) were purchased from Aladdin Reagents. In this work, all chemicals were of analytical grade and were purchased and used without further purification. Deionized water was used throughout the experiments.

2.2. Synthesis of CoMn-LDH

0.55 g of $\text{Co}(\text{NO}_3)_2 \bullet 6\text{H}_2\text{O}$ and 0.178 g of MnCl_2 were dissolved in 100 mL of deionized water, and then 0.32 g of NaOH and 0.32 g of Na_2CO_3 were dissolved in 30 mL of deionized water, and when the solution was dispersed uniformly, the solution containing Co^{2+} and Mn^{2+} was slowly added dropwise to the mixed solution of NaOH and Na_2CO_3 , then the mixed solution was transferred to an autoclave and heated at 120°C for 16 h. After cooling to room temperature, the solution was washed with deionized water three times and finally dried in an oven at 80°C for 12 h. The resulting product was named CoMn-LDH. In order to prove the superior properties of bimetal, the experiment of single metal hydroxide (Fig. S1)

2.3. Synthesis of CoMnLDH /ZIF-67

3.49 g of $\text{Co}(\text{NO}_3)_2 \bullet 6\text{H}_2\text{O}$ (0.01 mol) was added to the mixed solution of 20 mL methanol and 20 mL ethanol to obtain solution A. While 3.94 g of 2-methylimidazole and 0.01 g of cetyltrimethylammonium bromide were added to a mixture of 20 mL of methanol and 20 mL of ethanol to obtain solution B, (effect of ZIF-67 dosage on material capacity (Fig. S1). The two solutions were stirred and dissolved for 10 min then the appropriate amount of CoMn-LDHs was added to solution A and stirred for 30 min. Finally, solution A was slowly dripped into solution B with continuous stirring, followed by standing for 12 h. The resulting

product is CoMn-LDH/ZIF-67. ZIF-67 was synthesized as above, except that CoMn-LDHs were not added.

2.4. Synthesis of PANI

The purified 5 g aniline monomer was added into 20 mL 1.6 M HCl and dispersed by ultrasonic cleaning machine until the aniline and HCl were evenly mixed to obtain solution A. 6.134 g $(\text{NH}_4)_2\text{S}_2\text{O}_8$ was added to 20 mL 1.6 M HCl to obtain B solution, solution B was added to solution A drop by drop within 1 h, stirred continuously in the ice bath at 0°C for 24 h, filtered under pressure, and cleaned the cake with deionized water and ethanol. Finally, it is dried at 60°C for 24 h and ground to obtain the product.

2.5. Synthesis of CoMn-LDH /ZIF-67/PANI

To optimize the dosage of PANI added, 30, 40 and 50 mg PANI were dispersed in 20 mL DMF and sonicated for 1 h. PANI was added to a certain amount of CoMn-LDH/ZIF-67 and sonicated for 10 min. The mixture was then heated in a high-temperature reactor at 130°C for 48 h. After being cooled down to room temperature, the precipitates were washed with deionized water and anhydrous ethanol three times. Subsequently, the products were dried in an oven at 60°C for 10 h and recorded as CoMn-LDH/ZIF-67/PANI-3, CoMn-LDH/ZIF-67/PANI-4, and CoMn-LDH/ZIF-67/PANI-5.respectively.

2.6. Characterisation of materials

The crystal structure of the prepared electrode materials was determined by x-ray diffraction (XRD, BRUKER-AXS D8) in the range of $5\text{--}50^\circ$, and the surface morphology of the samples was observed in detail by scanning electron microscopy (SEM, S4-3400), and a transmission electron microscope (TEM, Talos F200 FEI). The elemental composition and valence states were determined on x-rays by photoelectron spectroscopy (XPS, AMATAB-MKII) using Mg K α x-ray radiation as an excited x-ray source, and the chemical composition and functional state of the composites were investigated by Fourier Transform Infrared Spectroscopy (FT-IR, Nicolet Avatar 380, Thermo Electron) with a wave number in the range of $(350\text{--}4000 \text{ cm}^{-1})$. The pore size, and specific surface of the synthesized composites were evaluated by Barrette Joyner Halenda (BJH) and Brunauere Emmette Teller (BET) techniques and evaluated on Quantachrome's NOVA2000e physical adsorption apparatus, tested after heating and degassing for 3 h at 180°C and 0.133 Pa pressure.

The electrochemical workstation used for the electrochemical tests was Shanghai Chenhua (CH1660E). 6 M KOH was used as the electrolyte in the three-electrode system, and the prepared material electrode was directly used as the working electrode, while the platinum piece and the mercuric oxide electrode were used as the auxiliary electrode and the reference electrode, respectively. Nickel foam was used as the collector.

Preparation of working electrodes: acetylene black was used as the conductive agent, and polytetrafluoroethylene (PTFE) was used as the binder. 5.2 mg CoMn-LDH/ZIF-67/PANI, 1 mg acetylene black, and 10 μL PTFE were added to 3 mL of ethanol and mixed by ultrasound for 40 min and then put into a blower oven and dried at 60°C overnight, and the paste-like material was uniformly coated on the treated nickel foam ($1 \times 1 \text{ cm}^2$) and pressurized under a pressure of 10 Mpa. The electrode active material load was approximately 3 mg cm^{-2} . The electrochemical performance of the prepared electrodes was evaluated using three test methods: cyclic voltammetry (CV), constant current discharge (GCD), and electrochemical impedance spectroscopy (EIS). The specific capacitance of the active material was obtained from equation [28,29] (1).

$$C_m = I \times t / (m \times \Delta V) \quad (1)$$

where C_m , I , t , m , and ΔV correspond to the specific capacitance of the

active substance (F g^{-1}), the current of constant-current charging, and discharging (A), the discharging time (s), the mass of the active substance (g), and the charging and discharging voltage (V), respectively.

In the two-electrode system, the CoMn-LDH/ZIF-67/PANI composite was used as the positive electrode, AC as the negative electrode, and 3 M KOH was used as the electrolyte. The amount of active substance and activated carbon can be calculated from the equation. (2).

$$\text{m}_+ / \text{m}_- = C_- \times \Delta V - /C_+ \times \Delta V + \quad (2)$$

The energy density (E) equation [30] of the asymmetric supercapacitor is calculated from Eq. (3) and the power density (P) is calculated from Eq. (4)

$$E = C_m \cdot (\Delta V)^2 / 7.2 \quad (3)$$

$$P = 3600E / \Delta t \quad (4)$$

In Eq. E is the energy density (Wh kg^{-1}); P is the power density (W Kg^{-1}); ΔV is the voltage window (V), C_m is the specific capacitance (F g^{-1}); and Δt is the discharge time (s).

3. Results and discussion

3.1. Material characterization

Fig. 1 shows the synthesis process of CoMn-LDH/ZIF-67/PANI. The specific surface area of the CoMn-LDH/ZIF-67/PANI composite is $371.78 \text{ m}^2 \text{ g}^{-1}$ (Fig. S3), which facilitates the contact of electrolyte with the active material, and is beneficial to improve the electrochemical properties of the material. The crystal structures of ZIF-67, CoMn-LDH, and CoMn-LDH/ZIF-67 were determined by XRD. As shown in Fig. 2(a), the diffraction peaks of ZIF-67 at 7.3° , 10.4° , 18° , and 26° can be attributed to the (011), (022), (222), and (134) crystal planes, ZIF-67 has good crystallinity (Fig. S4). The diffraction peaks appearing at 19.5° , 34° , and 38.7° for CoMn-LDH correspond to the (006) (012) (015) crystalline facets, respectively. The characteristic peaks of ZIF-67 and CoMn-LDH can be clearly observed in the XRD pattern of the prepared CoMn-LDH/ZIF-67 composite. It suggested that the CoMn-LDH/ZIF-67 was successfully synthesized.

Fourier transform infrared spectroscopy (FT-IR) in Fig. 2(b) shows the chemical composition and functional group composition of the prepared material. For ZIF-67, the peak at 1582 cm^{-1} is caused by the stretching and bending vibrations of the imidazole ring. In addition, the peak value at 2929 cm^{-1} was caused by the vibration of the aromatic nucleus of 2-methylimidazole. The above analysis confirmed the successful preparation of ZIF-67. The wide absorption band in the

$3400\text{--}3450 \text{ cm}^{-1}$ range is attributed to the O—H stretching vibrations of the water molecules. The peak at 400 cm^{-1} is caused by the bending vibration characteristic peak of the metal-oxygen (M—O) bond. CoMn-LDH has a strong peak at about 1000 cm^{-1} , which can be attributed to the characteristic peak caused by M—OH vibration. The peaks at 1638 cm^{-1} and 1367 cm^{-1} are attributed to the bending vibration of the interlayer H_2O and the antisymmetric stretching vibration of CO_3^{2-} , respectively. The above analysis confirmed the successful preparation of CoMn-LDH. The characteristic peaks of ZIF-67 and CoMn-LDH appear between 400 and 1600 cm^{-1} also appear in the corresponding spectra of CoMn-LDH/ZIF-67, indicating their successful combination in this composite. For CoMn-LDH/ZIF-67/PANI, the peaks at 1570 cm^{-1} and 1420 cm^{-1} correspond to the stretching vibration of quinone and benzene structures in the polyaniline chain, respectively. The peaks at 1291 cm^{-1} and 1120 cm^{-1} are the out-of-plane stretching vibration peaks of C—H and C—N on the benzene ring, respectively. The peak at 3439 cm^{-1} is the unsaturated N—H vibration absorption peak, so it can be proved that the addition of PANI has no great influence on its frame structure.

TEM images in Fig. 3 revealed the morphology and structure of the synthesized product of ZIF-67, CoMn-LDH, CoMn-LDH/ZIF-67, and CoMn-LDH/ZIF-67/PANI. As shown in Fig. 3(a), ZIF-67 possesses a rhombic dodecahedral structure and has a smooth surface. The average size of ZIF-67 is 200 nm. CoMn-LDH exhibits a typical nanosheet shape of metal hydroxide (Fig. 3(b)). The average size of CoMn-LDH is 200 nm. As shown in Fig. 3(c), ZIF-67 uniformly adheres to the surface of CoMn-LDH, and the addition of ZIF-67 makes the surface becomes rough. The CoMn-LDH/ZIF-67 composite was further proved to be a nanosheet shape of metal hydroxide by SEM (Fig. S5(c)). Fig. 3(d) shows the TEM of PANI added CoMn-LDH/ZIF-67, and it can be clearly observed that the PANI is well bonded on the composite. PANI acted as a "wire" to interconnect CoMn-LDH/ZIF-67 to form a network structure with a highly porous surface. Such a morphology provides more accessible active sites and promotes electron transfer. And it effectively improves the electrochemical performance of the material. Notably, the effective combination of CoMn-LDH/ZIF-67 and PANI avoids the stacking of CoMn-LDH and achieves a more stable structure and hence higher cycling stability (Fig. S5(d)). The EDS spectra of CoMn-LDH/ZIF-67/PANI are shown in Fig. 3(f)–(h). The characterization results show a uniform distribution of Co, Mn, C, N, and O elements in CoMn-LDH/ZIF-67/PANI, due to the inaccuracy of EDS light N content, we added XPS content determination. According to the analysis results, the content of nitrogen is about 16.54 %. According to the synthesis process of the final product. According to the proportion of raw materials added during the synthesis process, it can be divided into ZIF-67 (63.5 %), CoMn-LDH

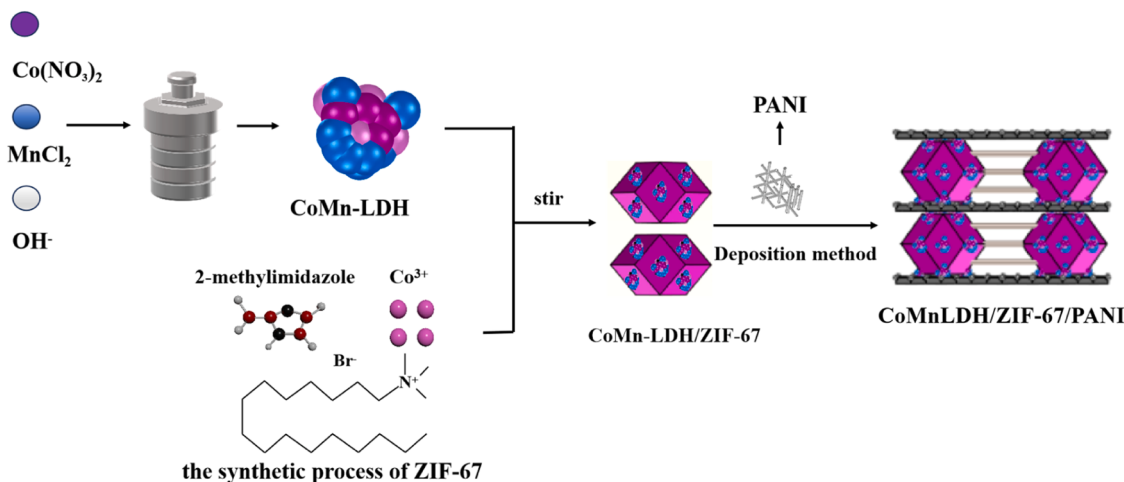


Fig. 1. Synthesis of CoMnLDH/ZIF-67/PANI.

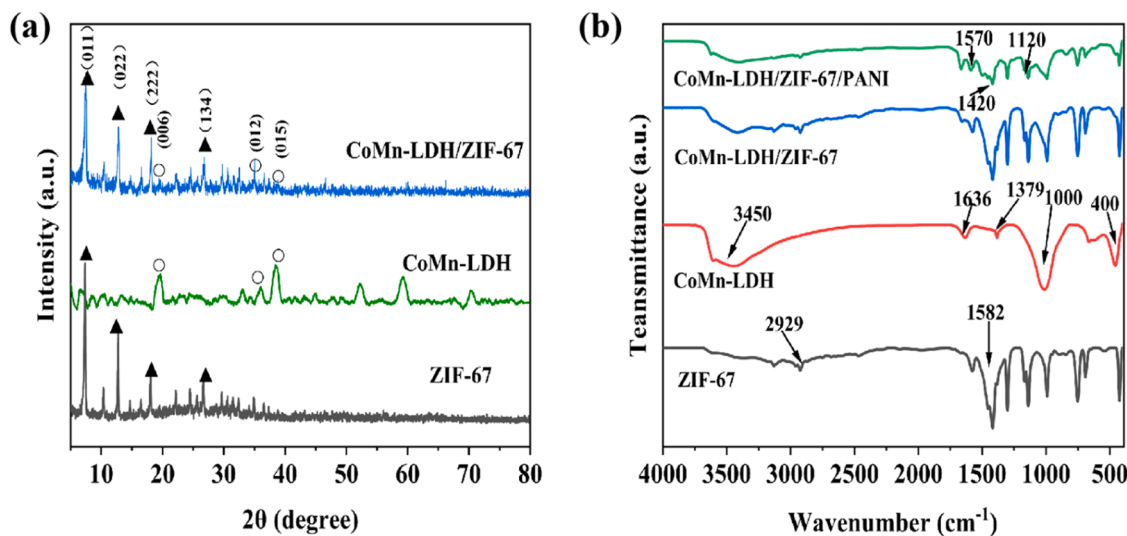


Fig. 2. (a) XRD patterns of ZIF-67, CoMn-LDH, and CoMn-LDH/ZIF-67; (b) FT-IR spectra of ZIF-67, CoMn-LDH, CoMn-LDH/ZIF-67 and CoMn-LDH/ZIF-67/PANI.

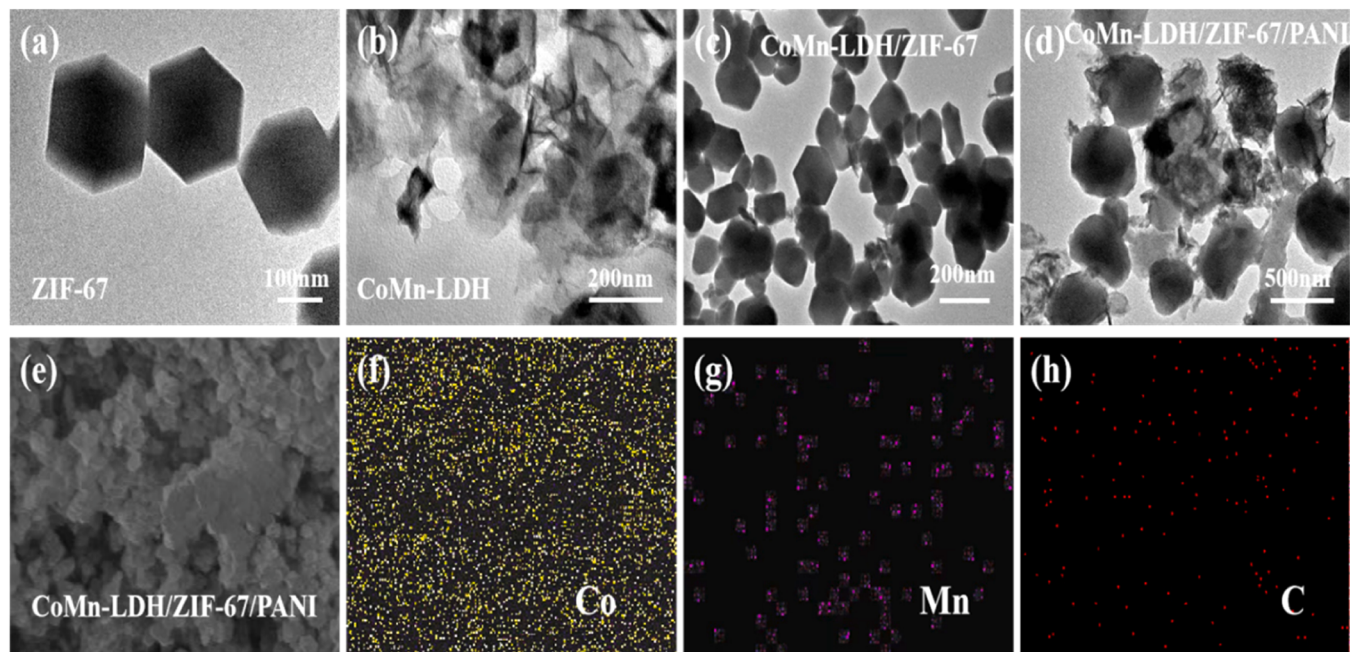


Fig. 3. TEM images of (a) ZIF-67, (b) CoMn-LDH, (c) CoMn-LDH/ZIF-67, (d) e–h) elemental mapping images of CoMn-LDH/ZIF-67/PANI.

(35.4 %), PANI (1 %), we calculate, in theory, the theoretical N content is calculated to be 16 %, it is basically consistent with the XPS test results, it is further proved that the material with the structure has been successfully synthesized by experiment.

The chemical composition and different elements' valence states of CoMn-LDH/ZIF-67/PANI were analyzed by XPS. As shown in Fig. 4(a), the full spectrum of CoMn-LDH/ZIF-67/PANI presents the Co, Mn, O, N, and C elements. There are two Co 2p_{1/2}, Co 2p_{3/2} main peaks and two satellite peaks in the Co 2p spectrum (Fig. 4(b)). The peaks with the binding energies of 780.6 and 796.4 eV are attributed to Co 2p_{3/2} and Co 2p_{1/2}, respectively, indicating the presence of Co³⁺ and Co²⁺. In the Mn 2p spectrum, two prominent peaks at 653.9 and 642.1 eV corresponded to Mn 2p_{1/2} and Mn 2p_{3/2}, indicating the presence of Mn³⁺ and Mn²⁺ (Fig. 4(c)). CoMn-LDH/ZIF-67/PANI has two types of oxygen located at 531.02 eV and 532.31 eV respectively as shown in Fig. 4(d). In the spectrum of N 1s, three peaks at 399.9 eV and 401.2 eV are

attributed to the quinone ring, benzene ring (—NH—), and N atom (—N+—) in the form of cationic free radicals (Fig. 4(e)). Among them, the characteristic peak of quinone ring is stronger than that of benzene ring, which also indicates that the oxidation state of PANI in the product is higher than that in the reduced state. The spectra of C1s show that the peaks at 287.9 eV, 285 eV, and 284.1 eV correspond to C=O, C—O, and C—C, respectively (Fig. 4(f)). Overall, these results are in good agreement with previous reports [31,32], showing that Co, Mn, O, N, and C elements coexist in CoMn-LDH/ZIF-67/PANI.

3.2. Electrochemical properties

In order to evaluate the electrochemical properties of the materials, CV, GCD, and EIS measurements were performed on all the prepared samples. Fig. 5(a) shows the CV curves of ZIF-67, CoMn-LDH, CoMn-LDH/ZIF-67, CoMn-LDH/ZIF-67/PANI-3, CoMn-LDH/ZIF-67/PANI-4,

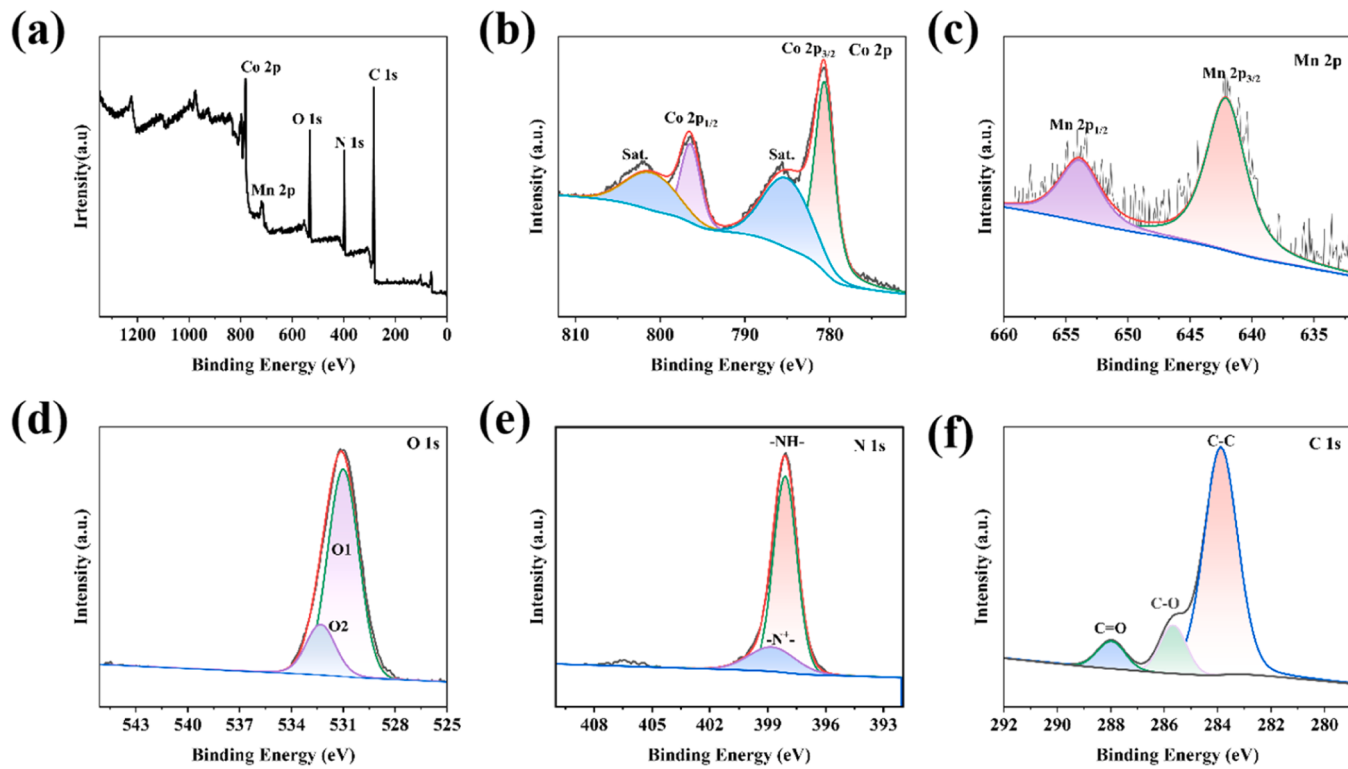


Fig. 4. XPS spectra of CoMn-LDH/ZIF-67/PANI composite. (a) Survey spectra of CoMn-LDH/ZIF-67/PANI composite, (b) Co 2p spectra, (c) Mn 2p spectra, (d) O1s spectra, (e) N 1s spectra, and (f) C1s spectra.

and CoMn-LDH/ZIF-67/PANI-5 under a voltage window of 0–0.6 V with a sweep speed of 10 mV s⁻¹. It can be seen that the oxidation and reduction peak currents of CoMn-LDH/ZIF-67/PANI-4 are higher than those of the other composites at the same scanning rate, and the larger the integrated area surrounded by the same sweep speed and the same potential window, the higher the specific capacitance of the material. It indicates that the composite CoMn-LDH/ZIF-67/PANI-4 has a higher specific capacitance than other materials.

Fig. 5(b) shows the galvanostatic charge/discharge (GCD) curves of the six electrode materials in 6 M KOH. With constant current charging/discharging in the potential range of 0–0.5 V and a current density of 1 A g⁻¹, the specific capacitors of ZIF-67, CoMn-LDH, CoMn-LDH/ZIF-67, CoMn-LDH/ZIF-67/PANI-3, CoMn-LDH/ZIF-67/PANI-4, and CoMn-LDH/ZIF-67/PANI-5 are 267.8, 286, 475.4, 840.2, 1048, and 635.8 F g⁻¹, respectively. It is worth noting that the specific capacitance of CoMn-LDH/ZIF-67/PANI-4 is significantly larger than that of the other materials, indicating that the performance is optimal when 40 mg PANI is incorporated into the material. Therefore, the combination of ZIF-67, CoMn-LDH, and PANI produces a synergistic effect that increases the resulting specific capacitance. The specific capacitances of the CoMn-LDH/ZIF-67/PANI composites are given in Table 1, along with comparisons with some other previously reported [33–37] CoMn-LDH-based, ZIF-67-based and PANI-based materials. As can be seen from Fig. 5(c), the rate performance of CoMn-LDH/ZIF-67/PANI is 61.07 %, while the other three materials are 49.1 %, 50.91 %, and 42.2 %, respectively, indicating that CoMn-LDH/ZIF-67/PANI electrode materials have excellent rate performance.

In order to further analyze the electrochemical properties of the electrodes, impedance tests were carried out to compare four electrode materials, ZIF-67, CoMn-LDH, CoMn-LDH/ZIF-67 and CoMn-LDH/ZIF-67/PANI (Fig. 5(d)). The electrochemical impedance spectroscopy (EIS) curves of the samples mainly consisted of a semicircle in the high and middle-frequency regions and a line in the low-frequency region. The semicircle in the high and middle-frequency regions is mainly

caused by the chemical reaction between the electrolyte and the cathode material, which represents the internal resistance (R_s) and interfacial charge transfer resistance (R_{ct}) in the high-frequency region. The line in the low-frequency region is an ion diffusion resistance. It can be found that the semicircle diameters of CoMn-LDH/ZIF-67/PANI are significantly smaller than those of the other materials, indicating its better charge transfer kinetics.

Fig. 6(a) is the CV curves of CoMn-LDH/ZIF-67/PANI under 5–40 mV s⁻¹ scan rates. As can be seen from Fig. 6(a), all the CV curves showed a pair of redox peaks, while the oxidation and reduction peaks were shifted to higher and lower potentials, respectively, with the increase of scan rates, which was a typical Faraday reaction. The GCD profiles of CoMn-LDH/ZIF-67/PANI are collected at different current densities within 0–0.5 V (Fig. 6(b)). The specific capacity capacitance is 1048 F g⁻¹ at 1 A g⁻¹, when the current density increases from 1 to 10 A g⁻¹, the specific capacitance decreases about 39 %. The excellent rate capability highlights the advantages of the CoMn-LDH/ZIF-67/PANI composite. The CoMn-LDH/ZIF-67/PANI electrode was determined by charge-discharge cycle voltammetry with a capacitance retention rate of 80.5 % after 3000 cycles (Fig. 6(c)). The slight increase in capacitance during the first 2500 cycles. This result is attributed to the increase of specific surface area and the increase of wettability during cycling to further improve the electrochemical performance.

Fig. 6(d) shows the specific capacitance of CoMn-LDH/ZIF-67/PANI at different current densities with specific capacities of 1048 F g⁻¹, 853.6 F g⁻¹, 793 F g⁻¹, 723 F g⁻¹ and 640 F g⁻¹ at 1, 2, 5, 8, 10 A g⁻¹, respectively. It can further prove that CoMn-LDH/ZIF-67/PANI samples have excellent rate performance.

In addition, the CV results were further analyzed to understand the charge storage mechanism of CoMn-LDH/ZIF-67/PANI. The peak current (i) and the scan rate (v) follow the power law relationship as follows [33–38].

$$i = av^b \quad (5)$$

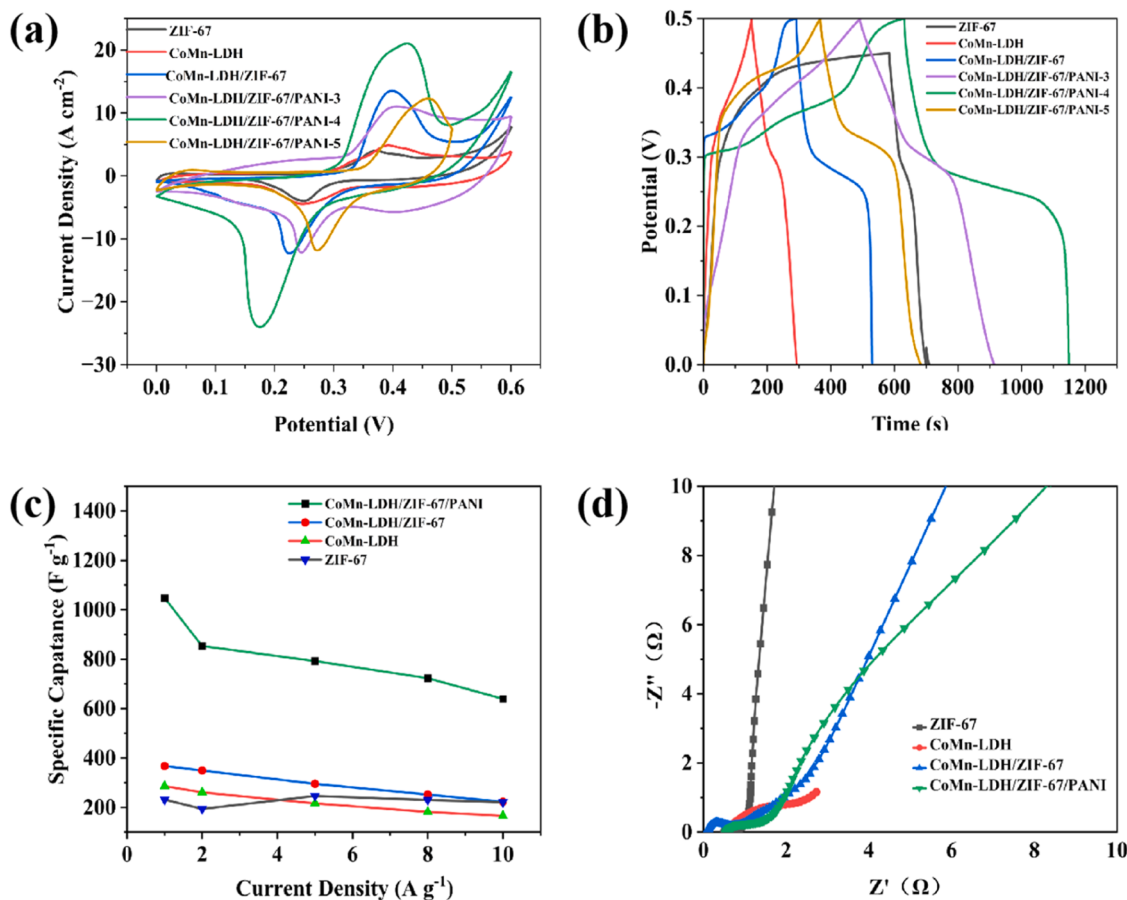


Fig. 5. (a) CV curves at 10 mV s^{-1} for different electrode materials, (b) GCD curves of different electrode materials at 1 A g^{-1} , (c) Specific capacitance of different electrode materials at current density 1 A g^{-1} , (d) EIS for different materials.

Table 1
Comparison of CoMn-LDH/ZIF67/PANI with Some Other CoMn-LDH-based, ZIF-67-based, and PANI-based electrode materials.

Electrode materials	Electrode specific capacitance (F g^{-1})	Electrolyte	Refs.
ZIF-67	230 (1 A g^{-1})	6 M KOH	[41]
ZIF-67/PPy	523 (1 A g^{-1})	6 M KOH	[42]
CoMn-LDH	173.9 (1 A g^{-1})	6 M KOH	[43]
Co-HKUST@CoMn-LDH	578.6 (1 A g^{-1})	6 M KOH	[44]
PANI	510 (1 A g^{-1})	6 M KOH	[45]
Ni-CeO ₂ @PANI	890 (1 A g^{-1})	6 M KOH	[46]
CoMn-LDH/ZIF67/PANI	1048 (1 A g^{-1})	6 M KOH	This work

where the a and b are both tunable parameters, in addition, b -value can be obtained from the relationship between $\log(i)$ and $\log(v)$. When the value of b is 0.5, the battery behavior is controlled by the diffusion process, and when the value of b is 1.0, it illustrates the capacitive behavior. The b values of CoMn-LDH/ZIF-67/PANI anode peak and cathode peak are about 0.605 and 0.517 respectively, which indicates that battery behavior is dominant in the energy storage mechanism (Fig. 6(d)). In addition, the diffusion contribution and capacitance contribution are further quantified according to Eq. (6) [18,39,40].

$$i(V) = k_1 v + k_2 v^{1/2} \quad (6)$$

where i and v are the total current response and scan rate under a fixed potential V , respectively, and k_1 and k_2 are constants that can be obtained by the relationship between $i/v^{1/2}$ and $v^{1/2}$. Then through $k_1 v$ and

$k_2 v^{1/2}$, the contribution from capacitance and diffusion control can be determined. It can be seen that the CoMn-LDH/ZIF-67/PANI electrode diffusion control process contributes 88.24 % to the total charge storage significantly higher than the capacitance contribution (Fig. 6(e)). In addition, the capacitive contribution gradually increases as the scan rate increases, and the diffusion control process is still dominant. These results indicate that CoMn-LDH/ZIF-67/PANI is a battery-type electrode material.

Figure S2 shows the electrode stability test curves of ZIF-67 and CoMn-LDH/ZIF-67 at 10 A g^{-1} , the capacitance retention of the ZIF-67 electrode is 65.3 % after 5000 cycles, however, CoMn-LDH/ZIF-67 has a capacitance retention rate of 75.1 %. This result proved that, CoMn-LDH can improve the cyclic stability due to the presence of Co-Mn dual active centers. The paper has room for improvement in the cycle stability, and the charging potential needs to be improved. If these problems are solved in the future, there will be more application prospects.

As shown in Fig. 6(f), the scan rate of the CoMn-LDH/ZIF-67/PANI electrode increased from 5 mV s^{-1} to 40 mV s^{-1} . With the increase of scan rate, the surface-controlled contribution increased, and the diffusion-controlled contribution decreased. This mainly depends on the charge storage mechanism. When the scan rate is increased, the electrolyte ions move rapidly and allow good penetration into the surface of the active material. As a result, a certain number of redox reactions take place on the material surface, but diffusion control still dominates. Therefore, CoMn-LDH/ZIF-67/PANI is a battery-type electrode material with obvious characteristics of battery-type electrode materials.

In order to explore the potential of CoMn-LDH/ZIF-67/PANI for practical applications, an asymmetric supercapacitor was constructed with the CoMn-LDH/ZIF-67/PANI composite material as the positive electrode and AC as the negative electrode. The operating voltages of AC

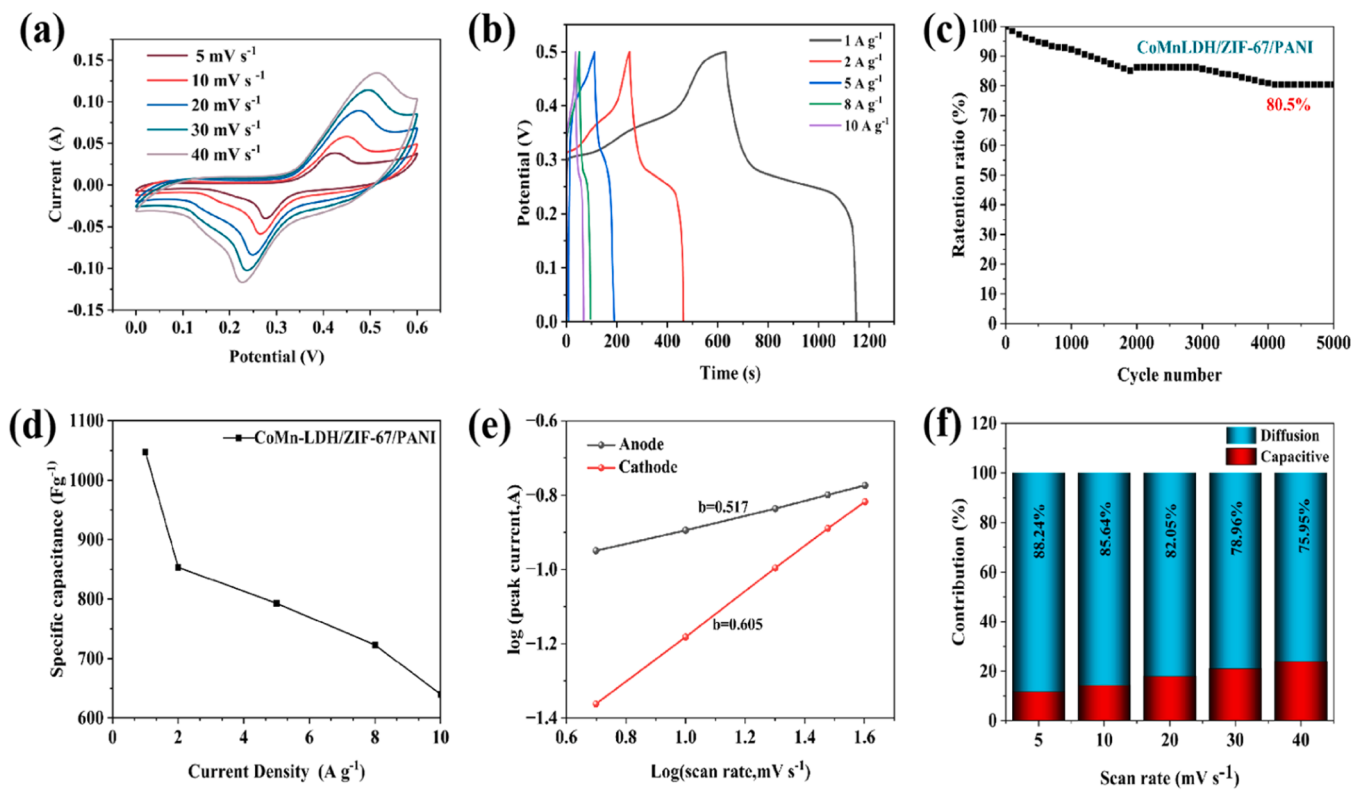


Fig. 6. (a) CV curves of CoMn-LDH/ZIF-67/PANI at different scan rates, (b) GCD curves of CoMn-LDH/ZIF-67/PANI at different current densities, (c) Cycling stability at a current density of 10 A g⁻¹, (d) Specific capacitance at different current densities, (e) The plot of log(i) versus log(v), (f) Relative contribution of diffusion and capacitance controlled charge storage at different scan rates.

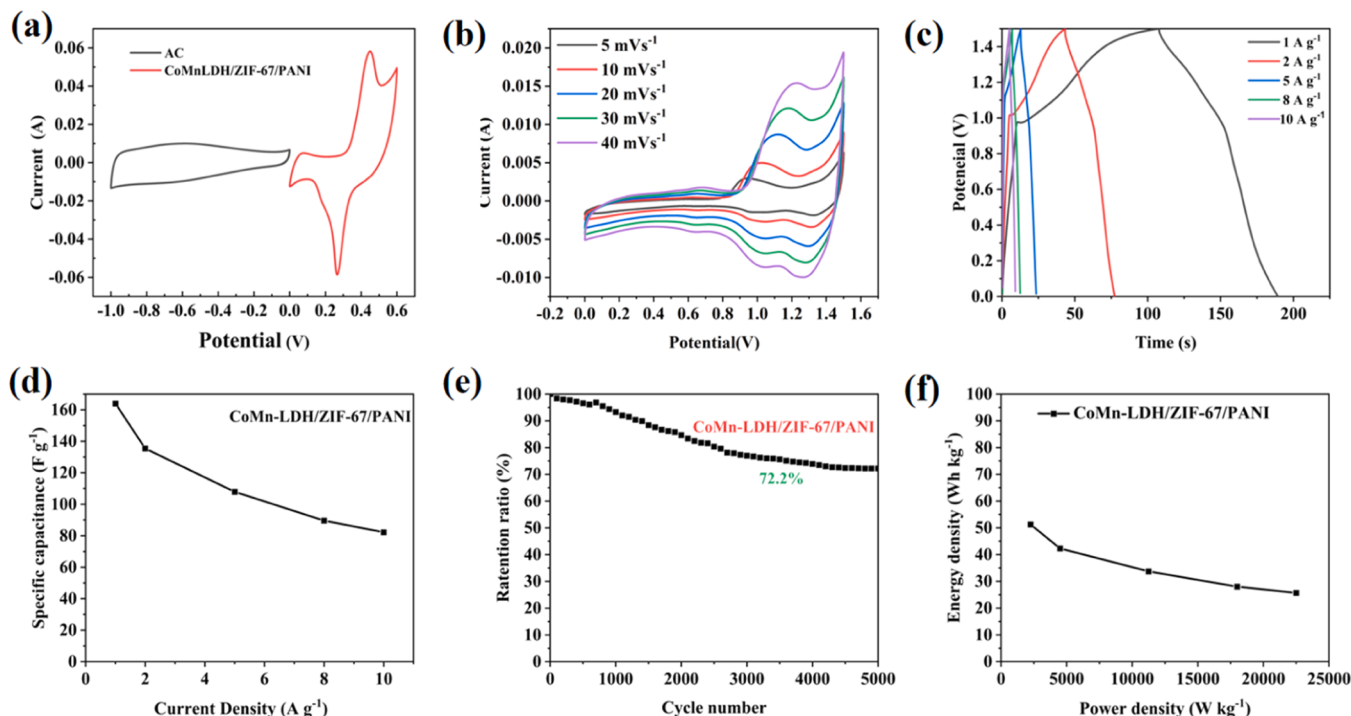


Fig. 7. (a) CV curves of AC and CoMn-LDH/ZIF-67/PANI electrodes at a scan rate of 10 mV s⁻¹, (b) CV curves at different scanning speeds, (c) GCD curves at different current densities, (d) Specific capacitance at different current densities, (e) Cycling performance at a current density of 10 A g⁻¹, (f) Power density versus energy density.

and CoMn-LDH/ZIF-67/PANI electrodes were in the ranges of $-1\text{--}0\text{ V}$ and $0\text{--}0.5\text{ V}$, respectively as shown in Fig. 7(a). $0\text{--}1.5\text{ V}$ was chosen as the potential window during the two-electrode test. Fig. 7(b) shows the CV curves of CoMn-LDH/ZIF-67/PANI//AC asymmetric supercapacitors at different sweep speeds., which change only slightly with the increase of the sweep rate, and the obvious redox peaks are evidence of the good reversibility and pseudocapacitance properties of the active materials. GCD curves of CoMn-LDH/ZIF-67/PANI//AC are exhibited in Fig. 7(c), and it can be seen that all the GCD curves are nonlinear, which is consistent with the results of CV curves. From the corresponding discharge time and Eq. (1), the specific capacitances of CoMn-LDH/ZIF-67/PANI at 1, 2, 5, 8, and 10 A g^{-1} are 164 F g^{-1} , 135.4 F g^{-1} , 107.9 F g^{-1} , 89.6 F g^{-1} , and 82.2 F g^{-1} , respectively, which further verifies that the specific capacitance of the CoMn-LDH/ZIF-67//AC is not linear. PANI//AC asymmetric supercapacitors with stable charge storage capacity.

From Fig. 7(d), it can be seen that the specific capacitance of CoMn-LDH/ZIF-67/PANI//AC, decreases with the increase of current density, but its rate performance can still reach 50.12 % after increasing from 1 A g^{-1} to 10 A g^{-1} . Thus, it can be concluded that CoMn-LDH/ZIF-67/PANI//AC asymmetric supercapacitors have good specific capacitance performance.

The cycling stability of CoMn-LDH/ZIF-67/PANI//AC was evaluated at a current density of 10 A g^{-1} (Fig. 7(e)). It was noteworthy that the capacitance retention rate can still reach 71.2 % after 5000 cycles, when reaches 1000 cycles, the specific capacities does not decrease but increases, this is due to the presence of the hydroxyl group in CoMn-LDH has a positive effect on the gradual wetting of the electrode, thereby extending the cycle life of the material. For CoMn-LDH can improve the cycle stability of the determination of the support material S2.

The Ragone plot of energy versus power density of the CoMn-LDH/ZIF-67/PANI//AC device is demonstrated as shown in Fig. 7(f). Using Eqs. (3) and (4), the energy density and power density of the device can be calculated. The ASC exhibits a relatively high energy density at a power density of 2250 W kg^{-1} of 51.25 Wh kg^{-1} , indicating that it is very valuable for applications.

4. Conclusions

In summary, CoMn-LDH/ZIF67/PANI nanocomposites with large surface areas were prepared, and their electrochemical energy storage properties were systematically investigated. The most appropriate content of PANI was forty percent in 1 g CoMn-LDH/ZIF67/PANI composite, which shows the best electrochemical performance. The specific capacitance of the CoMn-LDH/ZIF67/PANI electrode at a current density of 1 A g^{-1} reached 1048 F g^{-1} , and the capacitance was maintained at 80.5 % after 5000 cycles. In addition, the assembled asymmetric supercapacitors delivered an energy density of up to about 51.25 Wh kg^{-1} , and a power density of 2250 W kg^{-1} . The results show that the CoMn-LDH/ZIF67/PANI material has a broad application prospect in the field of electrochemistry.

CRediT authorship contribution statement

Jinyue Yang: Writing – original draft, Methodology, Investigation, Formal analysis. **Jianxin Wang:** Writing – review & editing, Supervision, Methodology, Funding acquisition, Conceptualization. **Chunhua Lou:** Investigation, Formal analysis. **Yuhan Cui:** Supervision, Methodology, Formal analysis, Conceptualization. **Xin Huang:** Methodology, Investigation. **Haixia Yu:** Methodology, Investigation, Formal analysis. **Liming Bai:** Methodology, Formal analysis. **Wendi Wang:** Investigation, Formal analysis. **Xinyou Zhang:** Formal analysis. **Hong Pan:** Writing – review & editing, Investigation, Formal analysis.

Declaration of competing interest

The authors declare that they have no known competing financial interests or personal relationships that could have appeared to influence the work reported in this paper.

Data availability

No data was used for the research described in the article.

Acknowledgment

This work was financially supported by the Education Department Basic Business of Heilongjiang (145209105).

Supplementary materials

Supplementary material associated with this article can be found, in the online version, at doi:10.1016/j.molstruc.2024.138392.

References

- [1] N. Gaulin, P. Le Billon, Climate change and fossil fuel production cuts: assessing global supply-side constraints and policy implications, *Clim. Policy* 20 (8) (2020) 888–901.
- [2] Ł. Mazur, S. Cieślik, S. Czapp, Trends in locally balanced energy systems without the use of fossil fuels: a review, *Energies* 16 (12) (2023) 4551.
- [3] R. York, L. Adua, B. Clark, The rebound effect and the challenge of moving beyond fossil fuels: a review of empirical and theoretical research, *Wiley Interdiscip. Rev.* 13 (4) (2022) e782.
- [4] S. Dahlgren, Biogas-based fuels as renewable energy in the transport sector: an overview of the potential of using CBG, LBG and other vehicle fuels produced from biogas, *Biofuels* 13 (5) (2022) 587–599.
- [5] P. Sharma, V. Kumar, Current technology of supercapacitors: a review, *J. Electron. Mater.* 49 (6) (2020) 3520–3532.
- [6] O.S. Adedoja, E.R. Sadiku, Y. Hamam, An overview of the emerging technologies and composite materials for supercapacitors in energy storage applications, *Polymers* 15 (10) (2023) 2272.
- [7] S. Kiruthika, N. Sneha, R. Gupta, Visibly transparent supercapacitors, *J. Mater. Chem. A* 11 (10) (2013) 4907–4936.
- [8] Z. Sun, K. Qu, Y. You, Z. Huang, S. Liu, J. Li, Q. Hu, Z. Guo, Overview of cellulose-based flexible materials for supercapacitors, *J. Mater. Chem. A* 9 (12) (2021) 7278–7300.
- [9] H. Li, K. Zhu, P.F. Wang, P. Liu, L. Jiao, Engineering of polyanion type cathode materials for sodium-ion batteries: toward higher energy/power density, *Adv. Funct. Mater.* 30 (28) (2020) 2000473.
- [10] M.U. Tahir, A. Sangwongwanich, D.I. Stroe, F. Blaabjerg, Overview of multi-stage charging strategies for Li-ion batteries, *J. Energy Chem.* 80 (26) (2023) 3009–7621.
- [11] D. Karimi, H. Behi, J. Van Mierlo, M. Berecibar, A comprehensive review of lithium-ion capacitor technology: theory, development, modeling, thermal management systems, and applications, *Molecules* 27 (10) (2022) 3119.
- [12] P. Hung, H. Zhang, H. Lin, Q. Guo, K.T. Lau, B. Jia, Specializing liquid electrolytes and carbon-based materials in EDLCs for low-temperature applications, *J. Energy Chem.* (68) (2022) 580–602.
- [13] Y. Wu, X. Wang, J. Shen, Metal oxide aerogels for high-temperature applications, *J. Sol-Gel Sci. Technol.* 106 (2) (2023) 360–380.
- [14] V. Gadore, S.R. Mishra, M. Ahmaruzzaman, Metal sulfides and their heterojunctions for photocatalytic degradation of organic dyes—A comprehensive review, *Environ. Sci. Pollut. Res.* 30 (39) (2023) 90410–90457.
- [15] R. Medhi, M.D. Marquez, T.R. Lee, Visible-light-active doped metal oxide nanoparticles: review of their synthesis, properties, and applications, *ACS Appl. Nano Mater.* 3 (7) (2020) 6156–6185.
- [16] A. Zadehnazari, Metal oxide/polymer nanocomposites: a review on recent advances in fabrication and applications, *Polymer-Plastics Technol. Mater.* 62 (5) (2023) 655–700.
- [17] Z. Feng, H.N. Lim, I. Ibrahim, N.S. Gowthaman, A review of zeolitic imidazolate frameworks (ZIFs) as electrochemical sensors for important small biomolecules in human body fluids, *J. Mater. Chem. B* 11 (38) (2023) 9099–9127.
- [18] L.J. Li, C.H. Chu, O.Y. Yu, Application of zeolites and zeolitic imidazolate frameworks in dentistry—A narrative review, *Nanomaterials* 13 (22) (2023) 2973.
- [19] Z. Zhuang, D. Liu, Conductive MOFs with photophysical properties: applications and thin-film fabrication, *Nano-Micro Lett.* 1 (2) (2020) 1–32.
- [20] C. Li, L. Zhang, J. Chen, Recent development and applications of electrical conductive MOFs, *Nanoscale* 13 (2) (2021) 485–509.
- [21] S.N. Eustis, D. Radisic, K.H. Bowen, R.A. Bachor, M. Haranczyk, G.K. Schenter, M. Gutowski, Electron-driven acid-base chemistry: proton transfer from hydrogen chloride to ammonia, *Science* 319 (5865) (2008) 936–939.

- [22] Y.Z. Zhang, Y. Wang, Y.L. XIE, Porous Hollow Co₃O₄ with rhombic dodecahedral structures for high-performance supercapacitors, *Nanoscale* 6 (2020) 1354–1459.
- [23] P. Bobde, A.K. Sharma, D. Panchal, A. Sharma, R.K. Patel, R.S. Dhodapkar, S. Pal, Layered double hydroxides (LDHs)-based photocatalysts for dye degradation: a review, *Int. J. Environ. Sci. Technol.* 20 (5) (2023) 5733–5752.
- [24] N. Dewangan, W.M. Hui, S. Jayaprakash, A.R. Bawah, A.J. Poerjoto, T. Jie, A. Jangam, K. Hidajat, S. Kawi, Recent progress on layered double hydroxide (LDH) derived metal-based catalysts for CO₂ conversion to valuable chemicals, *Catal. Today*, 35 (6) (2020) 490–513.
- [25] X. Ju, Z. Yang, X. Duan, The new emerging MXene/LDHs nanocomposites: a critical review of synthesis strategies, morphological regulation, and application prospects, *Appl. Mater. Today* 3 (4) (2023) 101908.
- [26] Z. Chen, Q. Fan, M. Huang, H. Cölfen, Synthesis of two-dimensional layered double hydroxides: a systematic overview, *CrystEngComm* 24 (26) (2022) 4639–4655.
- [27] W. Ou, X. Ye, Y. Zhou, Recent advances in Ni (oxy) hydroxides and Ni sulfides catalysts for oxygen evolution reactions, *Coord. Chem. Rev.* 493 (2023) 215274.
- [28] H. Hu, B. Guan, B. Xia, X.W. Lou, Designed formation of Co₃O₄/NiCo₂O₄ double-shelled nanocages with enhanced pseudocapacitive and electrocatalytic properties, *J. Am. Chem. Soc.* 137 (16) (2015) 5590–5595.
- [29] J. Banerjee, K. Dutta, M.A. Kader, S.K. Nayak, An overview on the recent developments in polyaniline-based supercapacitors, *Polym. Adv. Technol.* 30 (8) (2019) 1902–1921.
- [30] J.A. Oyetade, R.L. Machunda, A. Hilonga, Functional impacts of polyaniline in a composite matrix of photocatalysts: an instrumental overview, *RSC Adv.* 13 (23) (2023) 15467–15489.
- [31] M. Abbas, A.M. Marti, A. Umer, M. Joy, Y.-C. Yang, S.-L. Wang, K.J. Balkus, Encapsulation of cobaltoceneum ions in a zeolite-like metal–organic framework, *New J. Chem.* 47 (46) (2023) 21159–21167.
- [32] C.F.G.C. Geraldes, M.M.C.A. Castro, J.A. Peters, Mn (III) porphyrins as potential MRI contrast agents for diagnosis and MRI-guided therapy, *Coord. Chem. Rev.* 445 (2021) 214069.
- [33] M. Abbas, S.F.B. Haque, Y. Tian, J.P. Ferraris, K.J. Balkus Jr., Organic–inorganic nanohybrids in supercapacitors, *Hybrid Nanomaterials: Biomedical, Environmental and Energy Applications* (2022) 359–383.
- [34] P. Bobde, A.K. Sharma, D. Panchal, Layered double hydroxides (LDHs)-based photocatalysts for dye degradation: a review, *Int. J. Environ. Sci. Technol.* 20 (5) (2023) 5733–5752.
- [35] S. Mu, Q. Liu, P. Kidkhunthod, X. Zhou, W. Wang, Y. Tang, Molecular grafting towards high-fraction active nanodots implanted in N-doped carbon for sodium dual-ion batteries, *Natl. Sci. Rev.* 8 (7) (2021) nwaa178.
- [36] Z. Huang, P. Luo, Q. Wu, H. Zheng, Constructing one-dimensional mesoporous carbon nanofibers loaded with NaTi₂(PO₄)₃ nanodots as novel anodes for sodium energy storage, *J. Phys. Chem. Solids* 161 (2022) 110479.
- [37] A. Sherryna, M. Tahir, Recent developments in layered double hydroxide structures with their role in promoting photocatalytic hydrogen production: a comprehensive review, *Int. J. Energy Res.* 46 (3) (2022) 2093–2140.
- [38] E.K. Arora, V. Sharma, Ravi A, S. gtap, A. Adhikari, J.K. Dash, P. Kumar, R. Patel, Polyaniline-based ink for inkjet printing for supercapacitors, sensors, and electrochromic devices, *Energies* 16 (18) (2023) 6716.
- [39] Q. Li, H. Wang, H. Yu, M. Fu, W. Liu, Q. Zhao, S. Huang, L. Zhou, W. Wei, X. Ji, Y. Chen, Engineering an ultrathin and hydrophobic composite zinc anode with 24 μm thickness for high-performance Zn batteries, *Adv. Funct. Mater.* 33 (40) (2023) 2303466.
- [40] T. Ramakrishna, P.G. Dhananjaya, C.V. Sainagesh, S. Reddy, S. Kumaraswamy, N. C. Surendranatha, A review: electrical and gas sensing properties of polyaniline/ferrite nanocomposites, *Sens. Rev.* 42 (1) (2022) 164–175.
- [41] M. Daniel, G. Mathew, M. Anpo, B. Neppolian, MOF based electrochemical sensors for the detection of physiologically relevant biomolecules: an overview, *Coord. Chem. Rev.* 468 (2022) 214627.
- [42] Y. Liang, J.C.H. Goh, Polypyrrole-incorporated conducting constructs for tissue engineering applications: a review, *Bioelectricity* 2 (2) (2020) 101–119.
- [43] P. Majumder, R. Gangopadhyay, Evolution of graphene oxide (GO)-based nanohybrid materials with diverse compositions: an overview, *RSC Adv.* 12 (9) (2022) 5686–5719.
- [44] Y. Du, X. Liu, L. Chen, S. Yin, Y. Xie, A. Li, X. Liang, Y. Luo, F. Wu, Y. Mei, D. Xie, 3D hierarchical fireproof gel polymer electrolyte towards high-performance and comprehensive safety lithium-ion batteries, *Chem. Eng. J.* 476 (2023) 146605.
- [45] F. Golgovici, L. Anicai, A. Florea, Electrochemical synthesis of conducting polymers involving deep eutectic solvents, *Curr. Nanosci.* 16 (4) (2020) 478–494.
- [46] L. Amidani, T. Dumas, D.K. Shuh, S.M. Butorin, C.J. Sahle, A. Longo, K. O. Kvashnina, Oxygen K-edge X-ray absorption spectra of ThO₂ and CeO₂: experiment, interpretation, and structural effects, *J. Phys. Chem. C* 127 (6) (2023) 3077–3084.